

Revisiting the mechanisms of thermal transport in vacancy-defective silicon

Xueyan Zhu^{1,2,*}, Jin Yang³, Junichiro Shiomi⁴, and Cheng Shao^{5,†}

¹*CAEP Software Center for High Performance Numerical Simulation, Beijing 100088, People's Republic of China*

²*Institute of Applied Physics and Computational Mathematics, Beijing 100088, People's Republic of China*

³*ZJU-UIUC Institute, College of Energy Engineering, Zhejiang University, Jiaxing, Haining, Zhejiang Province 314400, People's Republic of China*

⁴*Department of Mechanical Engineering, The University of Tokyo, 7-3-1 Hongo, Bunkyo, Tokyo 113-8656, Japan*

⁵*Thermal Science Research Center, Shandong Institute of Advanced Technology, Jinan, Shandong Province 250103, People's Republic of China*

(Received 1 July 2025; revised 14 September 2025; accepted 24 October 2025; published 15 December 2025)

Understanding heat conduction in defective silicon is crucial for electronics and thermoelectrics. Conventional understanding relies on the phonon gas picture, treating defects as scattering centers that reduce phonon lifetimes without altering frequencies and group velocities. We go beyond the phonon gas picture by employing the Wigner transport equation to investigate heat conduction in vacancy-defective silicon. Our findings reveal that, while thermal conduction in pristine silicon stems mainly from particlelike propagation of vibrational modes, wavelike tunneling becomes increasingly important in the presence of vacancies. Contrary to the conventional belief that defects only perturb mode lifetimes, we demonstrate that vacancies also diminish velocity operators—a dominant factor in thermal conductivity reduction, surpassing even the effect of lifetime shortening. Furthermore, incorporating anharmonic frequencies and anharmonicity-renormalized interatomic force constants shows that, while anharmonicity suppresses thermal conductivity in pristine silicon, this effect weakens with vacancy concentration and reverses to enhance conductivity. These findings challenge conventional knowledge and provide insights into thermal conduction in defective materials.

DOI: [10.1103/112\(21\)214313](https://doi.org/10.1103/112(21)214313)

I. INTRODUCTION

The thermal conductivity of silicon containing defects, such as vacancies, interstitials, and voids, is of vital technological importance in many application areas including thermal management of electronics [1] and thermoelectrics [2,3]. For perfect silicon, its thermal transport behavior can be well described by the phonon Boltzmann transport equation (BTE) [4,5], considering only phonon-phonon scattering mechanism, [6]. After defects are introduced, the reduction in thermal conductivity is conventionally attributed to the phonon-defect scattering [7–10]. A large amount of research has been focused on quantitatively assessing the defect scattering parameters [11–15]. The thermal conductivity of defective crystal is usually calculated by solving the BTE considering phonon-defect scattering, with the assumption that vibrational frequencies and phonon velocities do not change with the defect concentration. However, crystal containing defects breaks the symmetry, which is an intermediate phase between crystal and glass. As a result, the particlelike propagation and scattering of vibrational modes may not fully capture the heat transfer mechanism in defective crystals. Heat may also be transferred via wavelike tunneling between vibrational modes. In addition, unit cells cannot be well defined in defective crystals, which may lead to the changes in

vibrational frequencies and velocity operators. In this work, we explore thermal transport mechanisms beyond the BTE and consider the vacancy-induced changes in vibrational frequencies and velocity operators.

Recent advancements in thermal transport theories, such as the Wigner formulation of the transport equation (WTE) [16,17] and the quasi-harmonic Green-Kubo approximation [18], have refreshed our understanding of heat conduction mechanisms in solids. These theories can consider the interplay between disorder, anharmonicity, and quantum Bose-Einstein statistics, naturally incorporating both particlelike and wavelike conduction mechanisms. Based on these theories, thermal conductivities of complex crystals [19–26] and glasses [27–29] have been successfully predicted. By considering both population and coherence contributions to the thermal conductivity, the transition from crystal-like to glasslike heat conduction has been observed through tuning atomic structures [21]. Although these new theories have made significant progress in understanding the thermal transport behaviors in crystals and glasses, their applications in defective crystals are rarely considered. The WTE framework provides a more comprehensive picture of the scattering process than the BTE framework. It not only captures the depumping and repumping of populations included in the BTE, but also incorporates the destruction of coherences [17]. Our work is devoted to applying the WTE in the calculation of the thermal conductivity of silicon containing vacancies, seeking to gain a deeper understanding of the fundamental mechanisms that govern thermal conduction in defective crystals.

*Contact author: zhu_xueyan@iapcm.ac.cn

†Contact author: cheng.shao@iat.cn

In addition to the consideration of coherence contribution to thermal conductivity, thermal transport theory can be further improved by incorporating anharmonicity-renormalized frequencies, interatomic force constants (IFCs), and higher-order scatterings between vibrational modes. Jain [19] found that the anharmonicity-renormalized IFC leads to more than a twofold increase in the thermal conductivity of Tl_3VSe_4 at 300 K, which is offset by including four-phonon scattering processes. Xia *et al.* [20] showed that anharmonicity-induced hardening of frequencies reduces the scattering rates of acoustic modes, which compensates for the increase in scattering due to phonon population. These effects result in nearly temperature-independent thermal conductivities. Studies on silica by Zhu and Shao [27] suggested that both anharmonic theory and anharmonic vibrational frequencies enhance thermal conductivity compared with harmonic theory and harmonic vibrational frequencies. These investigations indicate that the anharmonicity induced changes in vibrational properties should be considered as a factor that may influence the calculation results of thermal conductivities.

Conventionally, the impact of defects in crystal on heat conduction has been modeled as the introduction of additional scattering centers, which reduces thermal conductivity by shortening vibrational lifetimes. The vibrational frequencies and group velocities are assumed to be unaffected by the defects. However, group velocities are expected to play a significant role in thermal conduction, as indicated by the formulation of thermal conductivity [10]. Experimental work

by Hanus *et al.* [30] showed that the speed of sound in PbTe decreases with the increase in the internal strain, which was found to be a dominant factor for the reductions in the thermal conductivity. Kargar *et al.* [31] observed a decrease in the velocity of acoustic phonons of Al_2O_3 crystals due to Nd atom doping. These findings highlight the need for a reassessment of the assumption of constant group velocities in defective crystals, and a deeper investigation on how group velocities are affected by defects.

In this work, we calculate the thermal conductivity of vacancy-defective silicon using the WTE, which accounts for both particlelike propagation and wavelike tunneling of vibrational modes. By performing normal mode decomposition (NMD) on trajectories from molecular dynamics (MD) simulations, anharmonic vibrational frequencies and lifetimes are obtained, inherently incorporating all orders of anharmonicity. Through a renormalization method, anharmonicity-renormalized IFCs are also calculated. The effect of anharmonicity on the thermal conductivity is investigated considering both anharmonic frequencies and IFCs. Furthermore, we investigate how vacancies alter velocity operators and phonon lifetimes to elucidate the dominant mechanism behind vacancy-induced thermal conductivity reduction in silicon.

II. THEORETICAL FORMULATIONS

In this work, thermal conductivity is calculated by the formula derived from the Wigner transport equation [16]:

$$k^{\alpha\beta} = k_p^{\alpha\beta} + \frac{\hbar^2}{k_B T^2 V} \sum_{\mathbf{k}} \sum_{s,s'} \frac{\omega(\mathbf{k})_s + \omega(\mathbf{k})_{s'}}{2} v^\alpha(\mathbf{k})_{s,s'} v^\beta(\mathbf{k})_{s',s} \\ \times \frac{\omega(\mathbf{k})_s f(\mathbf{k})_{0s} [f(\mathbf{k})_{0s} + 1] + \omega(\mathbf{k})_{s'} f(\mathbf{k})_{0s'} [f(\mathbf{k})_{0s'} + 1]}{4[\omega(\mathbf{k})_s - \omega(\mathbf{k})_{s'}]^2 + [\Gamma(\mathbf{k})_s + \Gamma(\mathbf{k})_{s'}]^2} \times [\Gamma(\mathbf{k})_s + \Gamma(\mathbf{k})_{s'}], \quad (1)$$

where $k_p^{\alpha\beta}$ is the populations term and the additional tensor is the coherences term. In the above equation, $\omega(\mathbf{k})_s$ is the frequency of the s mode, $v^\alpha(\mathbf{k})_{s,s'}$ is the velocity operator along the α direction, $f(\mathbf{k})_{0s}$ is the equilibrium Bose-Einstein distribution, $\Gamma(\mathbf{k})_s$ is the linewidth of the s mode that is the inverse of the lifetime $\tau(\mathbf{k})_s$, \hbar is the reduced Planck constant, k_B is the Boltzmann constant, T is the temperature, and V is the volume. $k_p^{\alpha\beta}$ can be computed by the solution of the BTE. Under the relaxation time approximation, the calculation of $k_p^{\alpha\beta}$ can be simplified and the above equation becomes

$$k^{\alpha\beta} = \frac{\hbar^2}{k_B T^2 V} \sum_{\mathbf{k}} \sum_{s,s'} \frac{\omega(\mathbf{k})_s + \omega(\mathbf{k})_{s'}}{2} v^\alpha(\mathbf{k})_{s,s'} v^\beta(\mathbf{k})_{s',s} \\ \times \frac{\omega(\mathbf{k})_s f(\mathbf{k})_{0s} [f(\mathbf{k})_{0s} + 1] + \omega(\mathbf{k})_{s'} f(\mathbf{k})_{0s'} [f(\mathbf{k})_{0s'} + 1]}{4[\omega(\mathbf{k})_s - \omega(\mathbf{k})_{s'}]^2 + [\Gamma(\mathbf{k})_s + \Gamma(\mathbf{k})_{s'}]^2} \times [\Gamma(\mathbf{k})_s + \Gamma(\mathbf{k})_{s'}]. \quad (2)$$

The velocity operator $\mathbf{v}(\mathbf{k})_{s,s'}$ is defined by

$$v^\beta(\mathbf{k})_{s,s'} = e_\kappa^{\alpha*}(\mathbf{k})_s \nabla_{\mathbf{k}}^\beta \sqrt{D(\mathbf{k})}_{\kappa\alpha,\kappa'\alpha'} e_{\kappa'}^{\alpha'*}(\mathbf{k})_{s'}, \quad (3)$$

which can also be calculated by [16,32,33]

$$\mathbf{v}(\mathbf{k})_{s,s'} = \frac{i}{\omega(\mathbf{k})_s + \omega(\mathbf{k})_{s'}} \sum_{\alpha,\beta} \sum_{l,\kappa,\kappa'} e_\kappa^{\alpha*}(\mathbf{k})_s \frac{\Phi_{\kappa'\kappa}^{\beta\alpha}(0, l)}{\sqrt{m_\kappa m_{\kappa'}}} (\mathbf{R}_l + \mathbf{R}_{\kappa\kappa'}) e^{i\mathbf{k}\cdot(\mathbf{R}_l + \mathbf{R}_{\kappa\kappa'})} e_{\kappa'}^{\beta}(\mathbf{k})_{s'}. \quad (4)$$

In the above equation, $\Phi_{\kappa'\kappa}^{\beta\alpha}(0, l)$ is the non-Hermitian force constants, $e_\kappa^\alpha(\mathbf{k})_s$ is the phonon eigenvector, m_κ is the mass of

atom κ , \mathbf{R}_l is the position of cell l , and $\mathbf{R}_{\kappa\kappa'}$ is the distance between atom κ and atom κ' in a cell.

To obtain anharmonic vibrational frequencies and lifetimes, MD simulation-based NMD is carried out [34–36]. The trajectories of each atom from MD simulations are first projected onto the normal mode:

$$Q(\mathbf{k}, s, t) = \sum_{\alpha}^3 \sum_j^n \sum_l^N \sqrt{\frac{m_j}{N}} u_{jl}^{\alpha}(t) e_j^{\alpha*}(\mathbf{k})_s \exp(-i\mathbf{k} \cdot \mathbf{r}_{lj}), \quad (5)$$

in which N is the total number of unit cells, m_j is the mass of atom j , u is the displacement, and $e_j^{\alpha}(\mathbf{k})_s$ is the phonon eigenvector. Then, Fourier transform of the time derivative of the normal mode is conducted to obtain the spectral energy density (SED):

$$\Psi(\mathbf{k}, s, \omega) = |\mathcal{F}[\dot{Q}(\mathbf{k}, s, t)]|^2 = \left| \int_0^{+\infty} \dot{Q}(\mathbf{k}, s, t) e^{-i\omega t} dt \right|^2. \quad (6)$$

The anharmonic vibrational frequencies and lifetimes are obtained through fitting the SED by a Lorentzian function:

$$\Psi(\mathbf{k}, s, \omega) = \frac{C(\mathbf{k})_s}{[\omega - \omega^A(\mathbf{k})_s]^2 + [\Gamma(\mathbf{k})_s]^2}, \quad (7)$$

where ω is the harmonic frequency, ω^A is the anharmonic frequency, and Γ is the linewidth.

To consider the anharmonicity in the calculation of the thermal conductivity, both anharmonic frequencies and anharmonic interatomic force constants should be used. Anharmonic frequencies can be obtained through the above NMD method. The anharmonicity of force constants is considered through a renormalization method described below. The relationship between force constants and dynamical matrix is

$$\Phi_{0\kappa\alpha, l'\kappa'\alpha'} = \frac{\sqrt{m_\kappa m_{\kappa'}}}{N} \sum_{\mathbf{k}} D_{\kappa\alpha, \kappa'\alpha'}(\mathbf{k}) e^{-i\mathbf{k} \cdot (\mathbf{R}_{l'\kappa'}^0 - \mathbf{R}_{0\kappa}^0)}. \quad (8)$$

Considering that frequencies are eigenvalues of the dynamical matrix, the dynamical matrix can be computed by the following equation:

$$D_{\kappa\alpha, \kappa'\alpha'}(\mathbf{k}) = \sum_s e_{\kappa}^{\alpha}(\mathbf{k})_s \omega_{\mathbf{k}s}^2 e_{\kappa'}^{\alpha'*}(\mathbf{k})_s. \quad (9)$$

The anharmonicity-renormalized force constants are obtained through Eq. (8), in which the dynamical matrix is calculated by substituting anharmonic frequencies into Eq. (9).

III. COMPUTATIONAL DETAILS

MD simulations are performed using the LAMMPS package [37] to calculate the vibrational frequencies and lifetimes through lattice dynamics calculations and NMD method. The interaction energy between silicon atoms is calculated by the Tersoff interatomic potential [38]. The domain size is set to a $8 \times 8 \times 8$ conventional unit cell, with periodic boundary conditions applied in all three directions. Vacancies of concentrations 0.2, 0.5, 1.0, and 2.0% are introduced by randomly deleting silicon atoms.

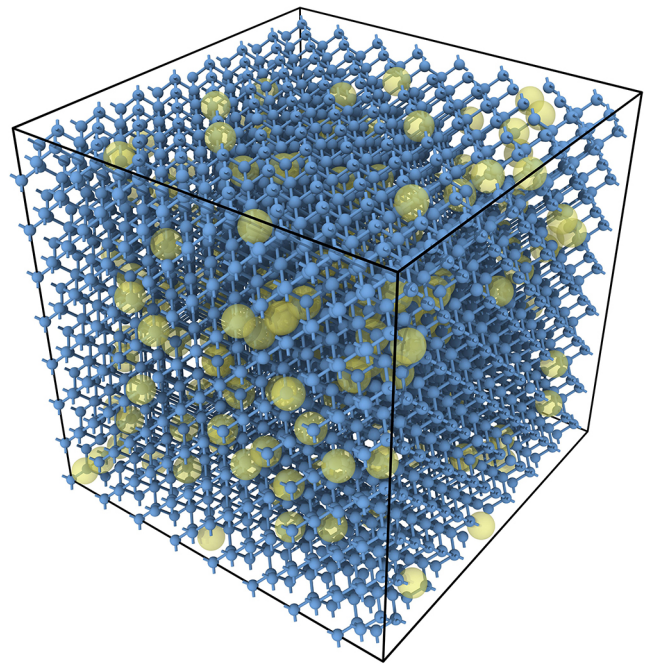


FIG. 1. Schematic of vacancy defects in silicon. Silicon atoms are depicted as blue spheres, while vacancies—randomly distributed within the silicon crystal lattice—are represented as semitransparent yellow spheres.

All the simulations are performed with periodic boundary conditions and a time step of 0.5 fs at 300 K. The system is first equilibrated for 1.5 ns in the *NPT* ensemble with the last 0.5 ns for averaging the box size. After setting the box size to the averaged value, the system is then simulated for 0.5 ns in the *NVT* ensemble and 1 ns in the *NVE* ensemble. The last frame of the above simulations is processed through an energy minimization for obtaining the equilibrium configuration.

Based on the equilibrium configuration, the system is equilibrated for 0.5 ns in the *NVT* ensemble and 0.5 ns in the *NVE* ensemble. Then, the velocities of each atom are dumped in the *NVE* ensemble for a time span of 5 ns, which are used for performing NMD.

Harmonic force constants are also calculated based on the equilibrium configuration. With the harmonic force constants and treating the total simulation box as a unit cell, lattice dynamics calculations are performed only at the Gamma point using the PHONOPY code [39] for obtaining the harmonic vibrational frequencies and eigenvectors.

IV. RESULTS

A. Thermal conductivity

Vacancy defects are randomly distributed in the silicon lattice as shown in Fig. 1. The variation of the thermal conductivity with respect to the vacancy concentration is depicted in Fig. 2. The increase in vacancy concentration leads to a rapid decrease in the thermal conductivity. Even with 0.2% vacancies, the thermal conductivity of the silicon decreases by 81.50%. The presence of 2.0% vacancies results in a 97.15% decrease in the thermal conductivity compared to perfect silicon. The results of this work are in good agreement with the

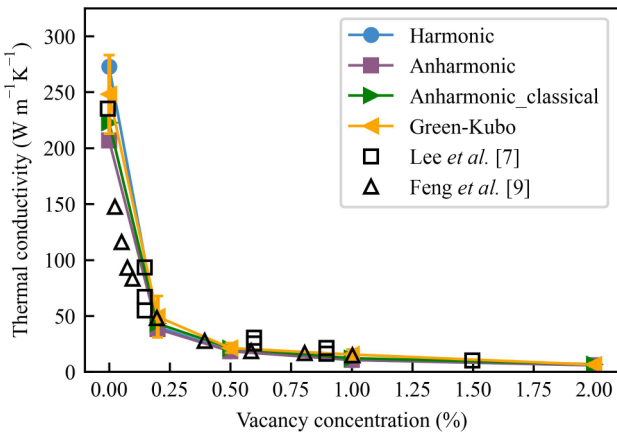


FIG. 2. Thermal conductivity of silicon as a function of vacancy concentration. The filled points represent data calculated by this work, while the hollow points correspond to data from MD simulations in the literatures [7,9]. The blue points correspond to data calculated based on Eq. (1) using harmonic frequencies and interatomic force constants (IFCs), while the purple points correspond to data calculated using anharmonic frequencies and anharmonicity-renormalized IFCs. The green points are obtained through Eq. (1) with Bose-Einstein statistics replaced by a classical one. The orange points are results of Green-Kubo method.

results of nonequilibrium MD simulations by Lee *et al.* [7] and Green-Kubo methods by Feng *et al.* [9] using the Tersoff potential. Although more accurate machine-learning-based interatomic potentials have been developed for predicting the thermal conductivity in pure silicon and silicon with vacancy defects [40], the primary focus of this work is to investigate the mechanisms by which vacancy defects impede thermal transport in silicon, rather than to obtain accurate thermal conductivity values. Therefore, we used the classical Tersoff potential to ensure computational efficiency and facilitate benchmarking against existing studies. To exclude the influence of artificial periodicity, thermal conductivities of both perfect sil-

icon and vacancy-defective silicon with different model sizes are calculated using the Green-Kubo method based on MD simulations as shown in the Supplemental Material [41]. It is found that a $5 \times 5 \times 5$ supercell is sufficient to achieve converged thermal conductivity. Based on the Green-Kubo method, a $8 \times 8 \times 8$ supercell is used to calculate thermal conductivities of silicon as a function of vacancy concentration. The results of the WTE with Bose-Einstein statistics replaced by a classical one (green points) are within the error bars of Green-Kubo results (orange points) as shown in Fig. 2.

Total thermal conductivity is decomposed into the contributions of populations and coherences. Since the crystal is treated as a large unit cell and only the Gamma point is considered in this work, exactly degenerate states do not exist. Quasidegenerate states with frequency differences smaller than 0.1 THz are regarded as degenerate states that contribute to the populations term. As shown in Fig. 3(a), the thermal conductivity contributed by the populations term decreases with the increase in the vacancy concentration, while the contribution from the coherences term first increases and then decreases. Figure 3(b) shows that the populations term dominates when the vacancy concentration is below 1.0%. In perfect crystal, the populations term contributes 99.91% of the total thermal conductivity. However, when the vacancy concentration exceeds 1.0%, the coherences term dominates. For silicon with 2.0% vacancy, the populations term contributes only 40.26% of the total thermal conductivity, while the coherences term contributes 59.74%. This indicates that, with the increase in vacancy concentration, heat transfer transits from particlelike propagation of the phonon wave packet to wavelike tunneling.

In addition, points corresponding to population contributions of 90 and 95% are marked in Fig. 3(b), and the corresponding vacancy concentrations are 0.057 and 0.025%, respectively. Therefore, to achieve accuracies of 90 and 95%, coherences contributions cannot be neglected when the vacancy concentration exceeds the concentration of 0.057 and 0.025%, respectively.

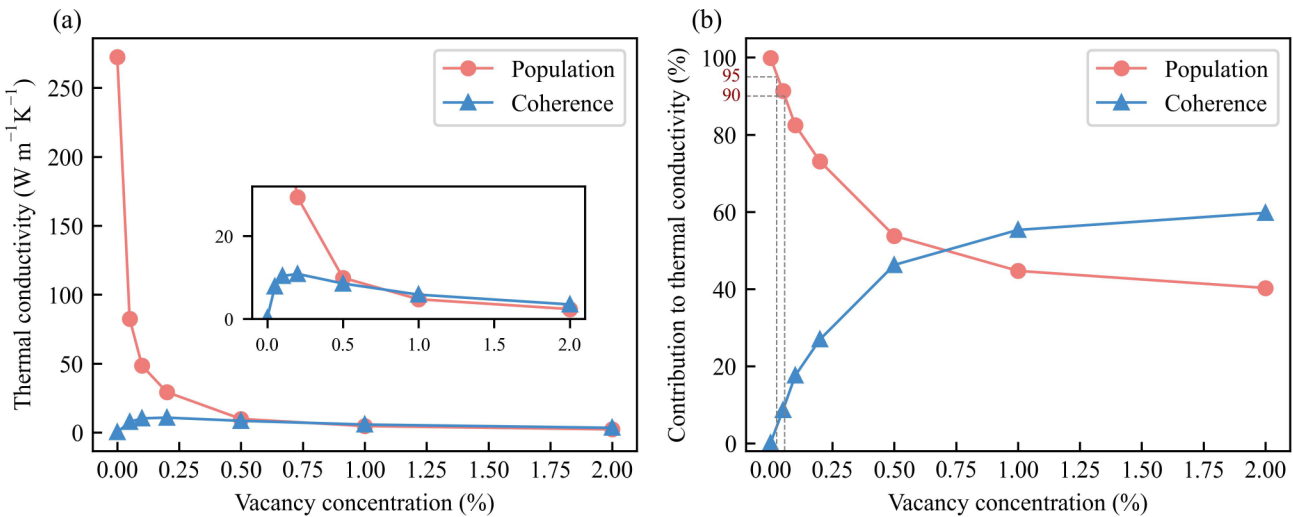


FIG. 3. Thermal conductivity decomposed into the populations and coherences terms. (a) Variation of the thermal conductivity contributed by the populations term and coherences term with respect to the vacancy concentration, respectively. (b) Relative contribution of the populations term and coherences term to the total thermal conductivity.

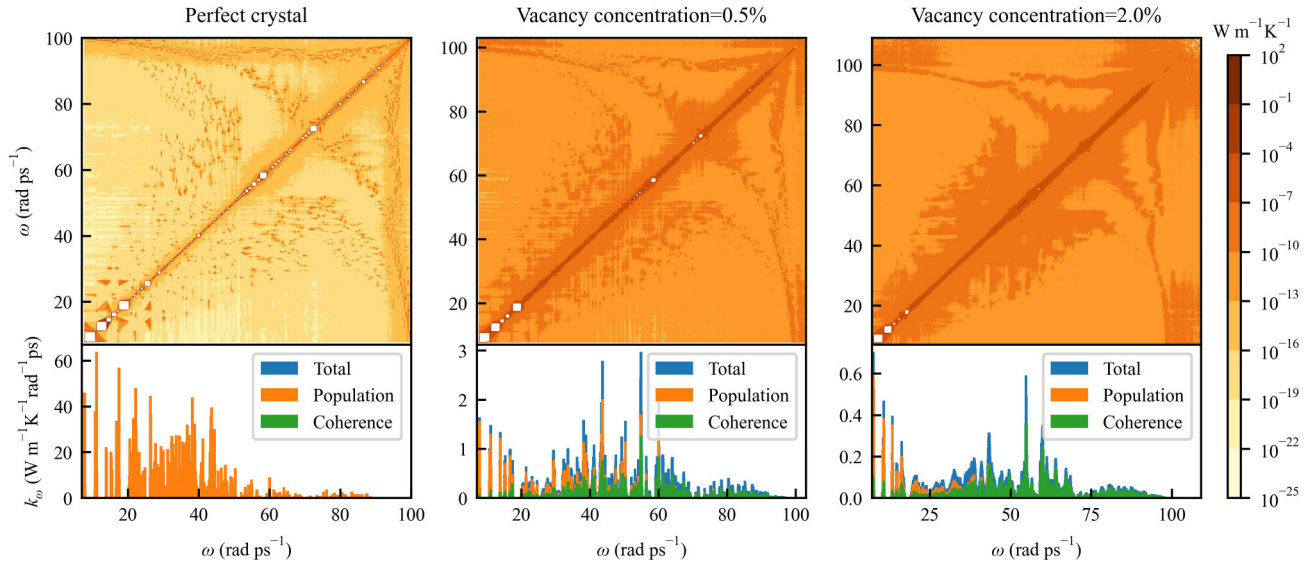


FIG. 4. Two-dimensional and one-dimensional frequency-dependent thermal conductivities. The one-dimensional frequency-dependent thermal conductivity is calculated by the formula $k_\omega = \sum_s k_s \delta(\omega_s - \omega)$ with the delta function approximated by the Gaussian function.

Figure 4 shows the frequency-dependent thermal conductivities, $k_{\omega\omega'}$ and k_ω , for perfect silicon and silicon containing vacancies, respectively. For perfect crystal, $k_{\omega\omega'}$ is mainly distributed near the diagonal and drops sharply away from the diagonal. With the increase in ω , the populations term of k_ω decreases rapidly. These results indicate that the thermal conductivity of perfect silicon is primarily contributed by quasidegenerate states at low frequencies. For silicon containing vacancies, the difference between $k_{\omega\omega'}$ near the diagonal and away from the diagonal becomes smaller compared with that in perfect silicon. The coherences term in vacancy-defective silicon is non-negligible, and mainly originates from the medium frequency spectrum of vibrational states, as indicated by the green bars in Fig. 4.

Figure 5 shows the cumulative coherence contribution up to a frequency cutoff calculated through the sum of all terms in Eq. (2) for which the frequency difference between modes

s and s' is less than the frequency cutoff. For perfect crystal, the curve nearly saturates at a frequency cutoff of 0.1 THz. This indicates the dominant role of coupling between quasidegenerate states in the thermal conduction of perfect silicon. As the vacancy concentration increases, the frequency cutoff required to achieve saturation also rises. This suggests that coherences between vibrational modes with larger frequency differences can participate in the thermal conduction as the vacancy concentration increases. However, the contribution of these coherences diminishes with increasing frequency differences, as evidenced by the decreasing slope of the curve with the frequency cutoff. Moreover, Fig. 5 reveals that even in silicon with 2.0% vacancies, 99% of the thermal conductivity originates from coherences between vibrational modes with frequency differences no larger than 1.3 THz. This indicates that in silicon containing vacancies, the coherences term of thermal conductivities is mainly contributed by the coherences between vibrational modes with small frequency differences. This finding is in agreement with previous investigations that the coherences contribution arising from structural disorder is predominantly due to couplings between states with small frequency differences [16,20].

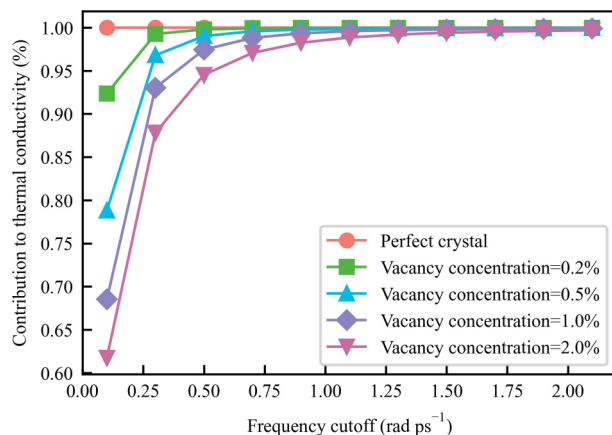


FIG. 5. Subcutoff coherence contribution to thermal conductivity divided by total thermal conductivity. The subcutoff coherence contribution is defined as the sum over all terms in Eq. (2) corresponding to mode pairs (s, s') the frequency difference of which is below a specified cutoff including both populations and coherences terms.

B. Anharmonicity

Thermal conductivities calculated using anharmonic frequencies and IFCs [purple line in Fig. 6(a)] are compared with those obtained through harmonic approximations [blue line in Fig. 6(a)]. The relative difference between the results of these two methods is shown by the purple line in Fig. 6(b). For perfect silicon, anharmonic effects induce a 24.18% suppression of the thermal conductivity. Notably, the influence of anharmonicity progressively attenuates with increasing vacancy concentration below 1.0%. Intriguingly, when the vacancy concentration reaches 1.0%, anharmonic contributions enhance thermal conductivity. This effect exhibits progressive amplification with increasing vacancy concentration, which is accompanied by the increase in the structural disorder. This

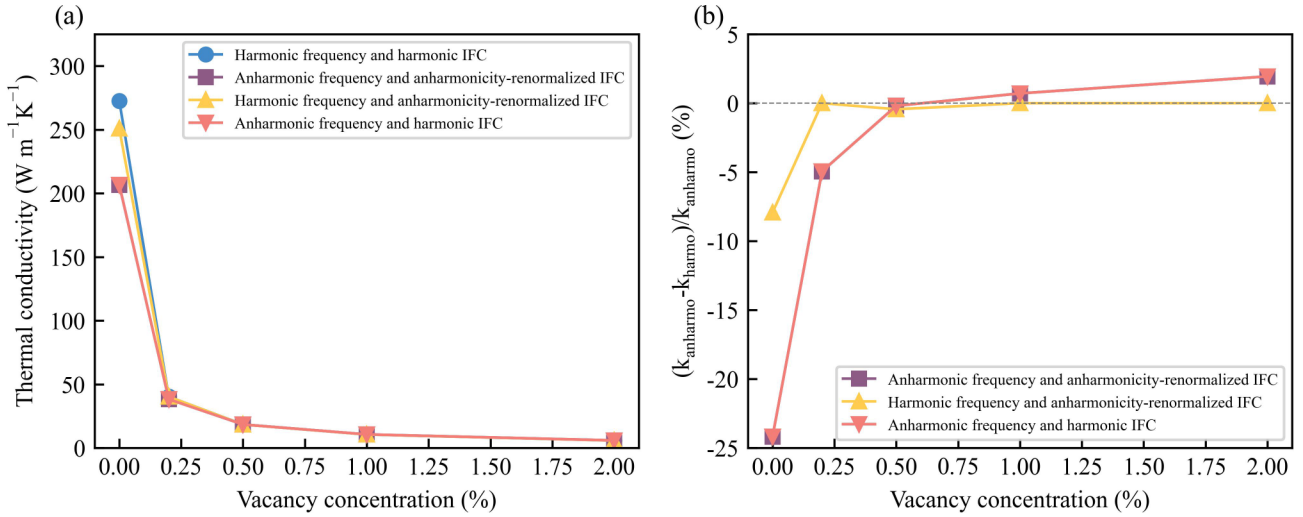


FIG. 6. (a) Comparison between thermal conductivities calculated using vibrational frequencies and IFCs with/without anharmonicity renormalized. (b) The relative differences between thermal conductivities arising from anharmonic and harmonic treatments of vibrational frequencies and IFCs. k_{harmo} is calculated using harmonic frequency and harmonic IFC. k_{anharmo} of the purple line is calculated using anharmonic frequency and anharmonicity-renormalized IFC. k_{anharmo} of the yellow line is calculated using harmonic frequency and anharmonicity-renormalized IFC. k_{anharmo} of the pink line is calculated using anharmonic frequency and harmonic IFC.

phenomenon aligns with our prior observations in the fully disordered amorphous silica system [27], wherein anharmonic interactions elevate thermal transport capabilities. These collective findings demonstrate that the role of anharmonicity in heat conduction undergoes a reversal—transitioning from detrimental suppression to beneficial enhancement—as material disorder evolves beyond the critical threshold.

A decoupling analysis is performed to isolate the individual effects of anharmonic frequency and anharmonicity-renormalized IFC on thermal conductivities. The investigation proceeds through two controlled computational experiments. First, while maintaining harmonic frequencies, thermal conductivity values computed with anharmonicity-renormalized IFCs are compared with those calculated using harmonic IFCs, as shown by the yellow line and blue line in Fig. 6(a). Their relative difference is shown by the yellow line in Fig. 6(b). The results show that considering only the anharmonicity-renormalized IFCs leads to a reduction of less than 10% in the thermal conductivity of defect-free Si, while the change in thermal conductivity for vacancy-containing Si is negligible. Second, thermal conductivity values obtained using anharmonic frequencies and harmonic IFCs are compared with those calculated using harmonic frequencies and harmonic IFCs, as shown by the pink line and blue line in Fig. 6(a). Their relative difference is shown by the pink line in Fig. 6(b). There is more than 20% reduction in the thermal conductivity of defect-free Si when using anharmonic frequencies. The pink line almost overlaps with the purple line. This reveals that the thermal conductivity modification induced solely by anharmonic vibrational frequencies exhibits comparable magnitude to the combined effects of anharmonic frequencies and anharmonicity-renormalized IFCs. Comparison between the yellow line and pink line demonstrates that implementing only anharmonicity-renormalized IFCs produces a significantly weaker thermal conductivity variation than the variation induced by isolated anharmonic frequency

adjustments. These findings demonstrate that frequency renormalization through anharmonic effects constitutes the primary mechanism governing anharmonicity-driven thermal conductivity modifications.

C. Mechanisms

To uncover the mechanism for heat transfer in silicon containing vacancies, Eq. (2) can be rewritten into the following form:

$$k^{\alpha\beta} = \frac{1}{V} \sum_{\mathbf{k}} \sum_{s,s'} C(\mathbf{k})_{s,s'} V^{\alpha}(\mathbf{k})_{s,s'} V^{\beta}(\mathbf{k})_{s,s'} \tau(\mathbf{k})_{s,s'}, \quad (10)$$

where

$$C(\mathbf{k})_{s,s'} = \frac{\omega(\mathbf{k})_s + \omega(\mathbf{k})_{s'}}{4} \left[\frac{C(\mathbf{k})_s}{\omega(k)_s} + \frac{C(\mathbf{k})_{s'}}{\omega(k)_{s'}} \right] \quad (11)$$

and

$$\tau(\mathbf{k})_{s,s'} = \frac{[\Gamma(\mathbf{k})_s + \Gamma(\mathbf{k})_{s'}]/2}{[\omega(\mathbf{k})_s - \omega(\mathbf{k})_{s'}]^2 + [\Gamma(\mathbf{k})_s + \Gamma(\mathbf{k})_{s'}]/4} \quad (12)$$

are defined as the two-mode heat capacity and lifetime [42], respectively. It has been verified that the effect of the vacancy concentration on the two-mode heat capacity is negligible. Therefore, it is sufficient to explore the vacancy-induced changes in the velocity operators and two-mode lifetimes to uncover the mechanisms of thermal transport degeneration in silicon containing vacancies.

Two-dimensional frequency-dependent velocity operators that have been diagonalized in degenerate subspaces are shown in Fig. 7. The contour map of velocity operators is similar to the contour map of thermal conductivities shown in Fig. 4. The maximum velocity is primarily concentrated around the diagonal. Away from the diagonal, only localized regions have relatively high velocities. With the increase in the vacancy concentration, velocities around the diagonal decrease, while those away from the diagonal increase.

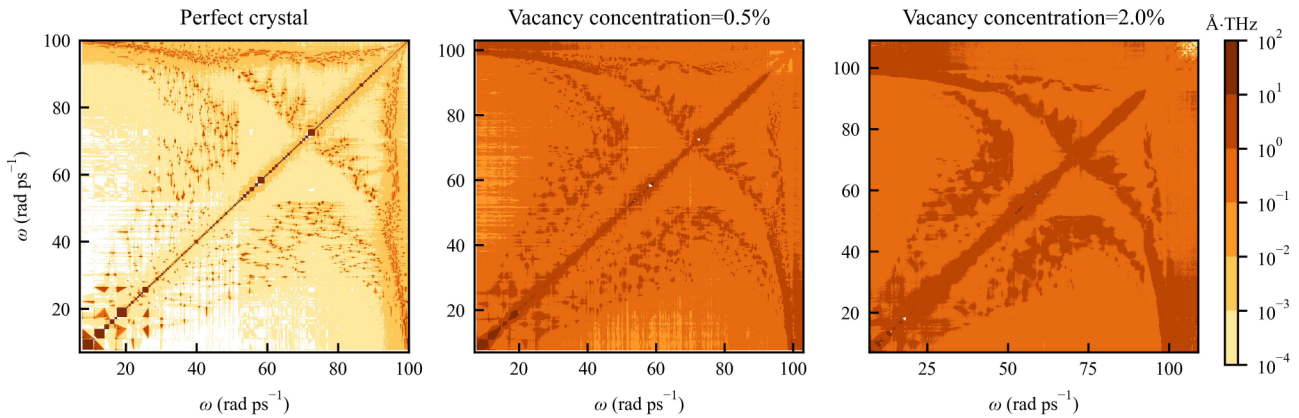


FIG. 7. Two-dimensional frequency-dependent velocity operators that have been diagonalized in the degenerate subspaces (collection of modes with the degenerate frequencies).

To quantitatively demonstrate how velocities vary with vacancy concentration, the velocities along the diagonal, as well as those deviating from the diagonal by 0.5 and 1 rad/ps, are plotted in Fig. 8. The velocity along the diagonal (offset = 0) that contributes to the populations term decreases rapidly as vacancy concentration increases. In contrast, the velocity deviating from the diagonal by 0.5 rad/ps first increases and then slightly decreases with increasing vacancy concentration. The velocity deviating from the diagonal by 1.0 rad/ps increases continuously with vacancy concentration.

The different effects of vacancies on the diagonal and off-diagonal velocity components arise from a shift of the heat transport mechanism from particlelike propagation to wave-

like tunneling and a reduction in IFCs. The decrease in velocity of the populations term as vacancy concentration increases is a result of the suppression of particlelike transport. The diagonal elements of the velocity operator represent the capability of a specific vibrational mode to transport energy by itself, corresponding to the classical group velocity in the particlelike (phonon gas) picture. In a perfect crystal, vibrational modes are highly delocalized plane waves (traveling waves) that can propagate freely over long distances with minimal resistance, enabling highly efficient energy propagation. The introduction of vacancies breaks translational symmetry, scattering these waves and leading to spatial mode localization. A localized mode resembles a standing wave confined in

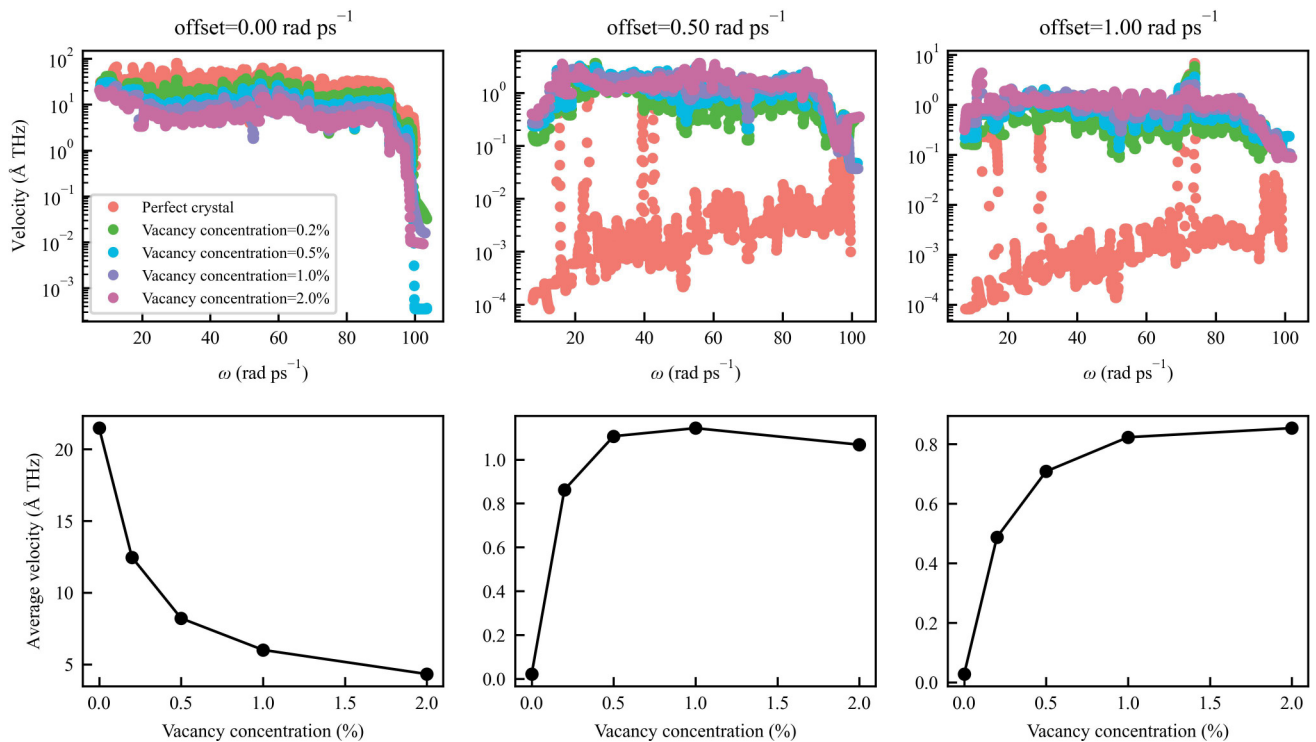


FIG. 8. Velocity operators along the diagonal (offset = 0), and those deviating from the diagonal by 0.5 and 1 rad/ps. The upper figures show the variation of the velocity with frequency, while the lower figures show the variation of the frequency-averaged velocity with vacancy concentration. The frequency-dependent velocity is calculated by the formula $v_\omega = \sum_s v_s \delta(\omega_s - \omega) / \sum_s \delta(\omega_s - \omega)$ with the delta function approximated by the Gaussian function.

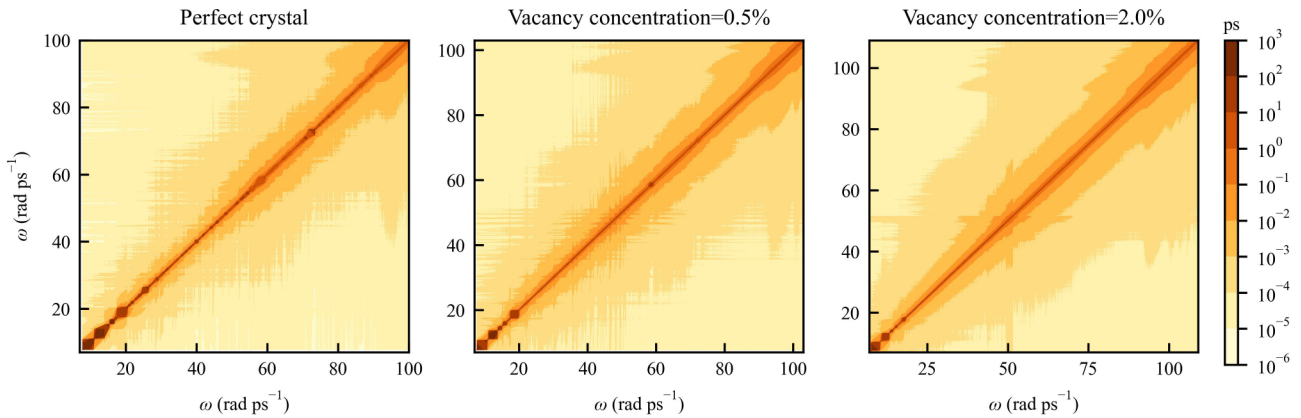


FIG. 9. Two-dimensional frequency-dependent two-mode lifetimes.

space. Its ability to propagate energy is drastically reduced, thereby diminishing the diagonal elements of the velocity operator. In contrast, the off-diagonal elements increase with vacancy concentration. This is a result of the enhanced wave-like tunneling between different modes. These off-diagonal elements represent the coupling strength between different vibrational modes and quantify the efficiency of energy tunneling from one mode to another. In perfect crystal, the coupling between different modes is almost zero. Vacancies create localized modes. These modes interact and couple through the interatomic forces. This coupling opens a new channel for energy transport: energy can be transferred between different modes, thus leading to an increase in the off-diagonal (coherence) term with rising vacancy concentration. Additionally, vacancies reduce IFCs due to broken bonds, which further suppresses the velocity—affecting both diagonal and off-diagonal elements of the velocity operator.

From Fig. 8, it is also found that the average velocity for perfect silicon along the diagonal is 21.46 Å/THz, which decreases to 0.02 Å/THz for a deviation of 0.5 rad/ps. However, for silicon with 2.0% vacancies, the average velocity only decreases from 4.32 to 1.07 Å/THz when the frequency deviates from the diagonal by 0.5 rad/ps. These results indicate that the diagonal elements dominate the velocity operator, and this dominance decreases as vacancy concentration increases. The difference between the diagonal and off-diagonal elements of the velocity operator shrinks with the increase in the vacancy concentration. These findings reveal that vacancy-induced changes in the velocity operators may serve as a key contributor to thermal conductivity reductions.

Figure 8 also shows how velocity varies with frequency. The diagonal velocity decreases as the frequency increases. For the velocity deviating from the diagonal by 0.5 and 1 rad/ps, it first increases to values oscillating around a constant at a frequency of approximate 20 rad/ps, and then decreases at a frequency of around 85 rad/ps. These results indicate that the populations term, associated with diagonal velocities, is mainly contributed by the low-frequency modes, while the coherences term, related to off-diagonal velocities, is mainly contributed by modes with intermediate frequencies.

The contour map of the two-mode lifetimes calculated by Eq. (12) is plotted in Fig. 9. The maximum two-mode lifetime is concentrated along the diagonal. As the distance from the diagonal increases, the two-mode lifetime decreases.

However, it is difficult to discern from the contour map how the two-mode lifetimes vary with the vacancy concentration and frequency.

To quantitatively demonstrate how two-mode lifetimes vary with the vacancy concentration and frequency, the two-mode lifetimes along the diagonal, as well as those deviating from the diagonal by 0.5 and 1 rad/ps, are plotted in Fig. 10. Both the diagonal and off-diagonal elements of the two-mode lifetimes decrease as the vacancy concentration increases. With the increase in the frequency, the diagonal lifetimes decrease. For off-diagonal lifetimes, they first increase to values around a constant, and then decrease with the frequency. This behavior is similar to the variation of velocity with the frequency described above, which further supports the finding that low-frequency modes dominate the particlelike propagation and the coherences term of wavelike tunneling is mainly contributed by modes with intermediate frequencies.

The above computational results demonstrate vacancy concentration-dependent behaviors in both velocity operators and phonon lifetimes, suggesting dual mechanisms for thermal conductivity reduction. To decouple these effects, we perform comparative calculations of thermal conductivities as a function of vacancy concentration: (1) varying velocity operators under fixed lifetimes and (2) changing lifetimes with constant velocity operators. The results are shown in Fig. 11. The vacancy-induced changes in velocity operators exhibit larger impacts on thermal conductivity reductions compared to lifetime suppression mechanisms. This finding challenges the long-standing defect scattering paradigm in phonon transport theory.

To provide an intuitive demonstration of the differences between the computational algorithm adopted in this manuscript and traditional phonon-scattering theory, comparisons are made between the results of this work and those calculated by the traditional BTE. In the traditional BTE, the phonon properties are usually assumed to be unchanged by the defects, and phonon-defect scattering parameters are calculated from the perturbation theory. The total phonon lifetime is calculated according to Matthiessen's rules $\tau^{-1} = \tau_{ph}^{-1} + \tau_d^{-1}$, where τ_{ph} is the lifetime due to phonon-phonon scattering and τ_d is the lifetime due to phonon-defect scattering. Only three-phonon scattering is considered for the calculation of τ_{ph} using the ALAMODE package [43]. The phonon-defect scattering rates are calculated using the mass perturbation approach proposed

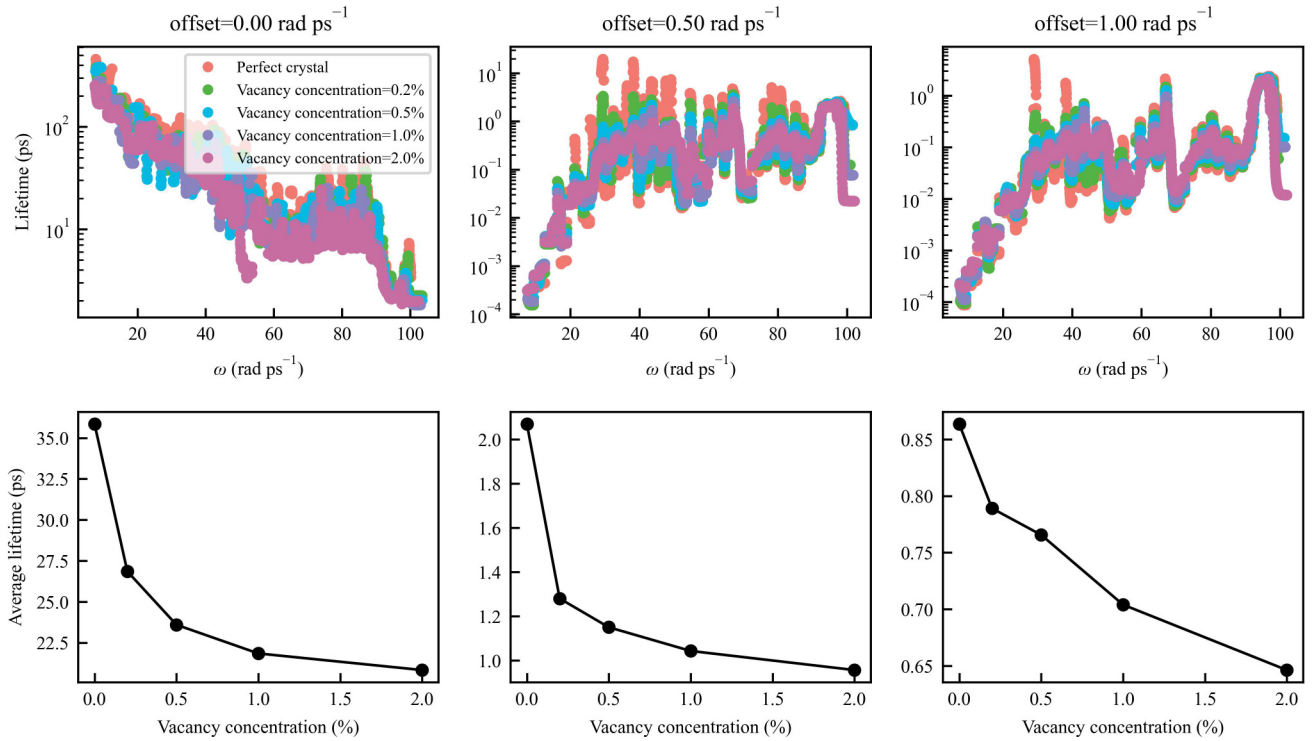


FIG. 10. Two-mode lifetimes along the diagonal (offset = 0), and those deviating from the diagonal by 0.5 and 1 rad/ps. The upper figures show the variation of the two-mode lifetime with frequency, while the lower figures show the variation of the frequency-averaged two-mode lifetime with vacancy concentration. The frequency-dependent lifetime is calculated by the formula $\tau_\omega = \sum_s \tau_s \delta(\omega_s - \omega) / \sum_s \delta(\omega_s - \omega)$ with the delta function approximated by the Gaussian function.

by Tamura [13]:

$$\tau_d^{-1}(\mathbf{k})_s = \frac{\pi}{2N} \omega^2(\mathbf{k})_s \sum_{\mathbf{k}', s'} \delta(\omega(\mathbf{k})_s - \omega(\mathbf{k}')_{s'}) \times \sum_{\kappa} g_{\kappa} |e_{\kappa}^*(\mathbf{k}')_{s'} \cdot e_{\kappa}(\mathbf{k})_s|^2, \quad (13)$$

$$g_{\kappa} = \sum_i f_{i,\kappa} \left(\frac{\bar{M}_{\kappa} - m_{i,\kappa}}{\bar{M}_{\kappa}} \right)^2 \quad (14)$$

where f_i and m_i are the fraction and the mass of the i th isotope atom, and $\bar{M}_{\kappa} = \sum_i f_{i,\kappa} m_{i,\kappa}$ is the average mass of atom κ . For vacancy scattering, the perturbation comes from both missing mass and missing bond. According to the virial theorem, potential-energy perturbations caused by missing bond are equal to the kinetic-energy perturbations caused by missing mass. Therefore, the perturbations at a vacancy site can be represented by the mass difference $\bar{M}_{\kappa} - m_{i,\kappa} = -m_{\text{vac}} - 2\bar{M}_{\kappa}$, in which m_{vac} is the mass of the vacant atom [15]. For achieving convergence of the calculation of the thermal conductivity [44], a $40 \times 40 \times 40 k$ mesh is used.

The computational algorithm used in this work and the above described traditional BTE differ in many aspects. First, the Wigner formalism used in this work includes both the populations term and coherences term. However, the traditional BTE ignores the coherences term. Second, the treatment of lifetimes and group velocities in this work differs from the traditional BTE. In this work, lifetimes are obtained through MD simulation-based NMD, which naturally considers all orders of scattering. The group velocities are calculated from the diagonal elements of velocity operators, which decrease with the increase in vacancy concentration. The traditional BTE usually only considers three-phonon scattering, and does not consider the change of group velocities by defects.

The thermal conductivity of pristine silicon calculated by the traditional BTE theory is 331.97 W/m/K, which is 21.78% higher than the result (272.60 W/m/K) of this work. This discrepancy can be attributed to the neglect of higher-order phonon scattering in the above BTE calculations.

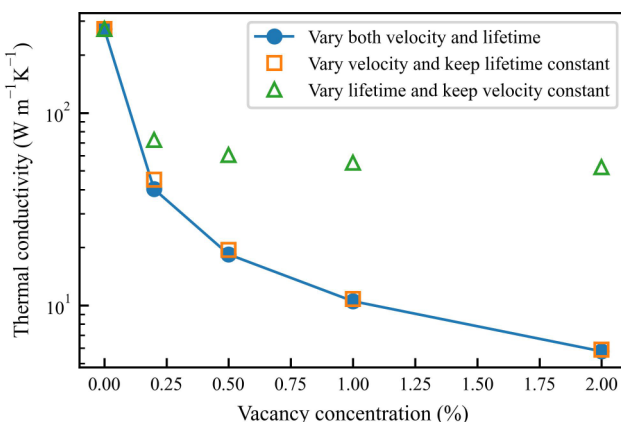


FIG. 11. Comparison of vacancy effects on thermal conductivities via independent changes of velocity operators and vibrational lifetimes. The hollow orange points show thermal conductivity vs vacancy concentration calculated by varying velocity operators under fixed lifetimes, while the hollow green points are obtained by changing lifetimes with constant velocity operators.

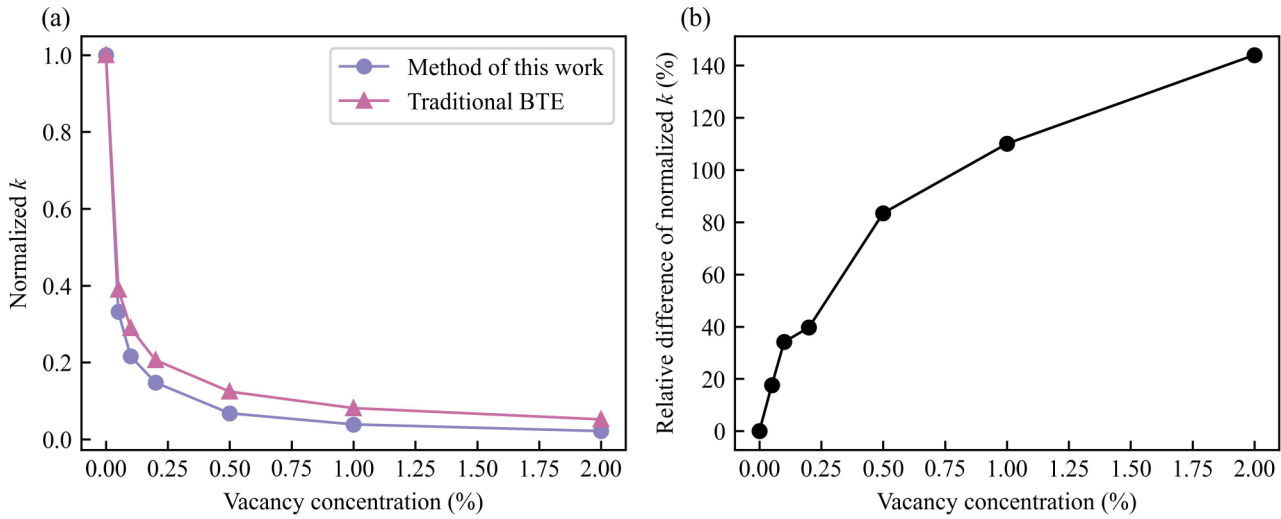


FIG. 12. (a) Comparison between the normalized k calculated through the method proposed in this work and the traditional BTE based on phonon-scattering theory. (b) The relative difference between the normalized k calculated by these two methods.

A comparison is made between the normalized thermal conductivity (ratio of vacancy-defective silicon's thermal conductivity to that of the pristine silicon) calculated through the method of this work and the traditional BTE [Fig. 12(a)]. Normalized k by the method of this work is smaller than that by the traditional BTE. With the increase in vacancy concentration, the relative difference between the normalized k calculated by these two methods becomes larger as shown in Fig. 12(b). When the vacancy concentration is smaller than 0.058%, the relative difference is smaller than 20%. Therefore, to ensure that the error is within 20%, the validation range for the traditional BTE theory to capture the vacancy effect on the thermal conduction reduction in silicon is < 0.058% vacancy concentration.

This larger normalized k predicted by the traditional BTE theory is mainly attributed to the use of phonon velocities of pristine silicon for the calculation of the thermal conductivity of vacancy-defective silicon. In this work, it is found that the diagonal elements of velocity operators diminish with the increase in vacancy concentration, which is a dominant factor that cannot be neglected for thermal conductivity reduction.

V. CONCLUSIONS

In conclusion, we investigated the thermal conduction in vacancy-defective silicon, considering both the particlelike propagation of vibrational modes and wavelike tunneling between modes. Our analyses incorporate anharmonic vibrational frequencies, anharmonicity-renormalized force constants, and vacancy-induced changes in both velocity operators and lifetimes. It is found that although the particlelike propagation dominates in defect-free silicon, wavelike tunneling becomes non-negligible in silicon containing vacancies. As vacancy concentration increases, wavelike tunneling becomes increasingly important. Further investigations on the frequency-dependent thermal conductivities, velocity oper-

ators, and lifetimes reveal that particlelike propagation is primarily contributed by the low-frequency modes, while the coherences term of wavelike tunneling is mainly contributed by modes with intermediate frequencies. Considering anharmonic frequencies and IFCs in the thermal conductivity calculations, we found that anharmonic effects suppress thermal conductivity in pristine silicon. However, increasing vacancy concentration progressively attenuates this anharmonic suppression, with a critical transition occurring at 1% concentration where the effect shifts from conductivity reduction to enhancement. To elucidate thermal transport mechanisms in vacancy-defective silicon, we systematically investigated vacancy-induced modifications in both velocity operators and vibrational lifetimes. Our analyses demonstrate that the observed thermal conductivity reduction arises predominantly from altered velocity operators, rather than lifetime shortening. This finding challenges the conventional knowledge that defects reduce thermal conductivity primarily through enhanced phonon scattering and reduced phonon lifetime, suggesting that current defect engineering strategies for thermal management may require reassessment. The revealed dominance of the phonon velocity reduction mechanism provides insights for developing thermal design methodologies.

ACKNOWLEDGMENT

This work was supported by National Natural Science Foundation of China (Grants No. 12005019 and No. 52306102).

DATA AVAILABILITY

The data that support the findings of this article are not publicly available. The data are available from the authors upon reasonable request.

- [1] A. L. Moore and L. Shi, Emerging challenges and materials for thermal management of electronics, *Mater. Today* **17**, 163 (2014).
- [2] D. Narducci and F. Giulio, Recent advances on thermoelectric silicon for low-temperature applications, *Materials* **15**, 1214 (2022).
- [3] N. S. Bennett, N. M. Wight, S. R. Popuri, and J.-W. G. Bos, Efficient thermoelectric performance in silicon nano-films by vacancy-engineering, *Nano Energy* **16**, 350 (2015).
- [4] R. E. Peierls, *Quantum Theory of Solids* (Oxford University, London, 1955).
- [5] J. Callaway, Model for lattice thermal conductivity at low temperatures, *Phys. Rev.* **113**, 1046 (1959).
- [6] T. Feng, L. Lindsay, and X. Ruan, Four-phonon scattering significantly reduces intrinsic thermal conductivity of solids, *Phys. Rev. B* **96**, 161201(R) (2017).
- [7] Y. J. Lee, S. Lee, and G. S. Hwang, Effects of vacancy defects on thermal conductivity in crystalline silicon: A nonequilibrium molecular dynamics study, *Phys. Rev. B* **83**, 125202 (2011).
- [8] T. Wang, G. K. H. Madsen, and A. Hartmaier, Atomistic study of the influence of lattice defects on the thermal conductivity of silicon, *Modell. Simul. Mater. Sci. Eng.* **22**, 035011 (2014).
- [9] T. L. Feng, B. Qiu, and X. L. Ruan, Coupling between phonon-phonon and phonon-impurity scattering: A critical revisit of the spectral Matthiessen's rule, *Phys. Rev. B* **92**, 235206 (2015).
- [10] R. Hanus, R. Gurunathan, L. Lindsay, M. T. Agne, J. Shi, S. Graham, and G. Jeffrey Snyder, Thermal transport in defective and disordered materials, *Appl. Phys. Rev.* **8**, 031311 (2021).
- [11] P. G. Klemens, The scattering of low-frequency lattice waves by static imperfections, *Proc. Phys. Soc. A* **68**, 1113 (1955).
- [12] P. G. Klemens, Thermal resistance due to point defects at high temperatures, *Phys. Rev.* **119**, 507 (1960).
- [13] S. I. Tamura, Isotope scattering of dispersive phonons in Ge, *Phys. Rev. B* **27**, 858 (1983).
- [14] S. I. Tamura, Isotope scattering of large-wave-vector phonons in GaAs and InSb: Deformation-dipole and overlap-shell models, *Phys. Rev. B* **30**, 849 (1984).
- [15] R. Gurunathan, R. Hanus, M. Dylla, A. Katre, and G. J. Snyder, Analytical models of phonon-point-defect scattering, *Phys. Rev. Appl.* **13**, 034011 (2020).
- [16] M. Simoncelli, N. Marzari, and F. Mauri, Unified theory of thermal transport in crystals and glasses, *Nat. Phys.* **15**, 809 (2019).
- [17] M. Simoncelli, N. Marzari, and F. Mauri, Wigner formulation of thermal transport in solids, *Phys. Rev. X* **12**, 041011 (2022).
- [18] L. Isaeva, G. Barbalinardo, D. Donadio, and S. Baroni, Modeling heat transport in crystals and glasses from a unified lattice-dynamical approach, *Nat. Commun.* **10**, 3853 (2019).
- [19] A. Jain, Multichannel thermal transport in crystalline Tl_3VSe_4 , *Phys. Rev. B* **102**, 201201(R) (2020).
- [20] Y. Xia, V. Ozoliņš, and C. Wolverton, Microscopic mechanisms of glasslike lattice thermal transport in cubic $Cu_{12}Sb_4S_{13}$ tetrahedrites, *Phys. Rev. Lett.* **125**, 085901 (2020).
- [21] E. Di Lucente, M. Simoncelli, and N. Marzari, Crossover from Boltzmann to Wigner thermal transport in thermoelectric skutterudites, *Phys. Rev. Res.* **5**, 033125 (2023).
- [22] A. I. Krivchikov, Y. V. Horbatko, O. A. Korolyuk, O. O. Romantsova, O. O. Kryvchikov, D. Szewczyk, and A. Jezowski, Exponential approximation of the coherence contribution to the thermal conductivity of complex clathrate-type crystals, *Materialia* **32**, 101944 (2023).
- [23] Z. Chang, J. Zheng, J. Ma, X. Zhang, Y. Gao, and D. Tang, Temperature-dependent interatomic force constants and phonon coherent resonance contribution in quaternary non-centrosymmetric chalcogenides $BaAg_2SnSe_4$, *Int. J. Heat Mass Transfer* **219**, 124863 (2024).
- [24] M. Simoncelli, D. Fournier, M. Marangolo, E. Balan, K. Béneut, B. Baptiste, B. Doisneau, N. Marzari, and F. Mauri, Temperature-invariant crystal-glass heat conduction: From meteorites to refractories, *Proc. Natl. Acad. Sci. U.S.A.* **122**, e2422763122 (2025).
- [25] J. Yue, J. Zheng, J. Li, S. Guo, W. Ren, H. Liu, Y. Liu, and T. Cui, Ultralow glassy thermal conductivity and controllable, promising thermoelectric properties in crystalline $o\text{-CsCu}_5S_3$, *ACS Appl. Mater. Interfaces* **16**, 20597 (2024).
- [26] Z. Z. Zeng, Z. Y. Fan, M. Simoncelli, C. Chen, T. Liang, Y. Chen, G. Thornton, and B. Q. Cheng, Lattice distortion leads to glassy thermal transport in crystalline $Cs_3Bi_2I_6Cl_3$, *Proc. Natl. Acad. Sci. USA* **122**, e2415664122 (2024).
- [27] X. Y. Zhu and C. Shao, Effect of anharmonicity on the thermal conductivity of amorphous silica, *Phys. Rev. B* **106**, 014305 (2022).
- [28] M. Simoncelli, F. Mauri, and N. Marzari, Thermal conductivity of glasses: First-principles theory and applications, *npj Comput. Mater.* **9**, 106 (2023).
- [29] A. F. Harper, K. Iwanowski, W. C. Witt, M. C. Payne, and M. Simoncelli, Vibrational and thermal properties of amorphous alumina from first principles, *Phys. Rev. Mater.* **8**, 043601 (2024).
- [30] R. Hanus *et al.*, Lattice softening significantly reduces thermal conductivity and leads to high thermoelectric efficiency, *Adv. Mater.* **31**, e1900108 (2019).
- [31] F. Kargar, E. H. Penilla, E. Aytan, J. S. Lewis, J. E. Garay, and A. A. Balandin, Acoustic phonon spectrum engineering in bulk crystals via incorporation of dopant atoms, *Appl. Phys. Lett.* **112**, 191902 (2018).
- [32] R. J. Hardy, Energy-flux operator for a lattice, *Phys. Rev.* **132**, 168 (1963).
- [33] P. B. Allen and J. L. Feldman, Thermal conductivity of disordered harmonic solids, *Phys. Rev. B* **48**, 12581 (1993).
- [34] M. T. Dove, *Introduction to Lattice Dynamics* (Cambridge University, New York, 1993).
- [35] A. J. H. McGaughey and J. M. Larkin, Predicting phonon properties from equilibrium molecular dynamics simulations, *Annu. Rev. Heat Transfer* **17**, 49 (2014).
- [36] C. Shao and J. Shiomi, Negligible contribution of inter-dot coherent modes to heat conduction in quantum-dot superlattice, *Mater. Today Phys.* **22**, 100601 (2022).
- [37] S. Plimpton, Fast parallel algorithms for short-range molecular dynamics, *J. Comput. Phys.* **117**, 1 (1995).
- [38] J. Tersoff, New empirical approach for the structure and energy of covalent systems, *Phys. Rev. B* **37**, 6991 (1988).
- [39] A. Togo and I. Tanaka, First principles phonon calculations in materials science, *Scr. Mater.* **108**, 1 (2015).
- [40] H. Babaei, R. Guo, A. Hashemi and S. Lee, Machine-learning-based interatomic potential for phonon transport in perfect crystalline Si and crystalline Si with vacancies, *Phys. Rev. Mater.* **3**, 074603 (2019).

- [41] See Supplemental Material at <http://link.aps.org/supplemental/10.1103/11h-kbv3> for size-dependent thermal conductivity from Green-Kubo method.
- [42] J. Yang, X. Zhu, A. J. H. McGaughey, Y. S. Ang, and W.-L. Ong, Two-mode terms in Wigner transport equation elucidate anomalous thermal transport in amorphous silicon, *Phys. Rev. B* **111**, 094206 (2025).
- [43] T. Tadano, Y. Gohda, and S. Tsuneyuki, Anharmonic force constants extracted from first-principles molecular dynamics: Applications to heat transfer simulations, *J. Phys.: Condens. Matter* **26**, 225402 (2014).
- [44] A. J. H. McGaughey *et al.*, Phonon olympics: Phonon property and lattice thermal conductivity benchmarking from open-source packages, *J. Appl. Phys.* **138**, 135108 (2025).